Available online at www.sciencedirect.com

ScienceDirect

Advances in Space Research xx (2023) xxx-xxx

ADVANCES IN SPACE RESEARCH (a COSPAR publication)

www.elsevier.com/locate/asr

GNSS-based Baseline Vector Determination for Widely Separated Cooperative Satellites Using L1-Only Receivers

Ahmed Mahfouz[a,*], Davide Menzio[b], Florio Dalla Vedova[c], Holger Voos[a,d]

[a] *SnT, University of Luxembourg, 29 Avenue John F. Kennedy, L-1855 Luxembourg, Luxembourg*
[b] *Former SnT, University of Luxembourg, 29 Avenue John F. Kennedy, L-1855 Luxembourg, Luxembourg*
[c] *LuxSpace, 9 Rue Pierre Werner, L-6832 Betzdorf, Luxembourg*
[d] *Faculty of Science, Technology and Medicine, University of Luxembourg, 2 Avenue de l'Université L-4365 Esch-sur-Alzette, Luxembourg*

Received 31 October 2023; Received in final form 20 June 2023; Accepted 21 June 2023;
Available online 10 July 2023

Abstract

Real time estimation of the relative position and velocity vectors between two satellites in a formation is an integral part of the formation control loop. Relative positioning based on Global Navigation Satellite Systems (GNSS) has been a dominating technology for formation missions in LEO, where extremely precise estimates could be obtained for formations with small inter-satellite distances ($1 - 10$ km). Larger baselines between the satellites (> 10 km) are more challenging as they pose the problem of huge differences in the ionospheric delays experienced by the signals received by each receiver. This problem could be mitigated by using precise ionospheric-free combinations that could only be obtained by dual-frequency receivers, which is not a cost-efficient option for the modern low-cost miniature missions. In this paper, the problem of GNSS-based relative navigation between two spacecraft with large inter-satellite distance which are equipped with single-frequency receivers is treated through adopting the space-proven Extended Kalman Filter (EKF). Although using an EKF for relative navigation is a common practice, there are many variants of the filter settings, which vary in terms of the state and measurement vectors to be adopted as well as the techniques to be used to handle the ionospheric delay. In this research, optimal settings of the filter are sought for the problem of relative baseline vector estimation between two spacecraft that have large separation and which are equipped with with single-frequency GNSS receivers.
© 2023 COSPAR. Published by Elsevier Ltd All rights reserved.

Keywords: Satellite formation ; DGNSS ; Relative navigation ; State estimation ; Extended Kalman Filter

1. Introduction

A reliable state estimation subsystem is essential to close the control loop for any control system. Satellites in Low Earth Orbits (LEO) have long relied on Global Navigation Satellite System (GNSS) signals to estimate their position and velocity vectors in real-time which enabled precise orbit maneuvers. Two distinctive GNSS-based positioning schemes are extricated, absolute positioning and relative positioning.

Absolute positioning aims at estimating the position vector of the receiver with respect to the center of the Earth, either by solely relying on the measurements from that receiver (standalone positioning) or by combining the measurements from the main receiver and another nearby stationary base receiver with a precisely known position. The latter leverages Differential GNSS (DGNSS) techniques and is not suitable for space applications since the existence of a base in space with a

*Corresponding author: Tel.: +352-661-76-3934;
Email address: Ahmed.mahfouz@uni.lu (Ahmed Mahfouz)

https://dx.doi.org/10.1016/j.jasr.xxxx.xx.xxx
0273-1177/© 2023 COSPAR. Published by Elsevier Ltd All rights reserved.

precisely known position and with a sustained communication link to the main receiver is an elaborate task. Relative positioning on the other hand is after estimating the baseline vector of one receiver with respect to another, conceivably using the GNSS signals collected by these receivers and also sometimes, leveraging DGNSS techniques. The accuracy of the absolute positioning schemes can vary from few centimeters to tens of meters Correa-Muños & Cerón-Calderón (2018); Le & Tiberius (2003) depending on many factors such as whether DGNSS is incorporated, atmospheric conditions, receiver quality and design features, and signal blockage. While absolute positioning is a natural choice for one-satellite missions, relative positioning can be essential for the multi-satellite ones.

Indeed, sensor sets other than GNSS receivers could be used to carry out relative navigation tasks for different mission scenarios. Schemes for relative navigation between two closely flying objects, either cooperative or non-cooperative, have been developed based on line of sight measurements Ardaens & Gaias (2018, 2019), LiDAR Woods & Christian (2016), GNSS receivers Montenbruck et al. (2002); Park et al. (2010, 2013), and both, cameras as well as GNSS receivers Capuano et al. (2022). However, GNSS sensors stand as the perfect choice for cooperative spacecraft, especially when the baseline between the flying satellites is large, where vision-based sensors could no longer capture the features of the target spacecraft.

GNSS-based Extended Kalman Filters (EKF) have shown to achieve superb estimates with millimeter-level accuracy of the baseline vector for formations with small inter-satellite distances ($1 - 10$ km) in Low Earth Orbits BUSSE et al. (2003); Leung & Montenbruck (2005); D'Amico et al. (2009). Baseline estimation has also been tackled for longer inter-satellite distances Kroes et al. (2005); Tancredi et al. (2014) and remarkable accuracies could be obtained using dual-frequency receivers. Dual-frequency receivers in the case of long baselines ($10 - 500$ km) are very important not only to mitigate the huge difference in ionospheric delay between the two receivers, but also to help fixing the double difference integer ambiguities. Nevertheless, the construction of precise relative orbit determination algorithms using single-frequency receivers shall be an enabling technology for low-cost satellites formations in LEO. In Giralo & D'Amico (2021), a hybrid Extended/Unscented Kalman Filter is proposed for baseline determination for widely spaced formations equipped with single-frequency GNSS receivers. The algorithm which performs double-difference integer ambiguity resolution could achieve excellent estimations of the baseline vector (2 cm RMS error) using GPS data that was generated by a GNSS receiver emulator for two spacecraft 500 km apart. Although fairly precise for large baselines, this algorithm suffers from slow convergence time (around 1 hour).

In this paper, relative navigation for satellite formations equipped with single-frequency GNSS receivers and with large inter-satellite distance ($10 - 500$ km) is investigated using an Extended Kalman Filter (EKF). In this setting, ionospheric delay is, in most cases, the largest bias that needs to be filtered out. A bi-linear ionospheric model is used in conjunction with ionospheric-free combinations to achieve relative state estimates without the need to perform integer ambiguity resolution.

The relative position and velocity between two spacecraft are to be estimated directly by the filter rather than estimating the absolute states then subtracting them from each other to obtain the baseline position and velocity, hence, nonlinear relative dynamics between the target and the chaser spacecraft are used. Single difference quantities are fed to the filter for their advantage of cancelling out common biases such as the instrumental delays of the commonly tracked satellites.

The work in this paper is an extension to our preliminary study Mahfouz et al. (2022) with a handful of modifications, the most important of which is the adoption of a more precise ionospheric model. Moreover, the state vector setup as well as the way of choosing the measurement variance-covariance matrix are modified.

This research comes as part of the AuFoSat project which aims at developing a toolbox that features autonomous constella-

tion and formation control solutions comprising state estimation and control algorithms. The toolbox is going to be used by LuxSpace which is currently developing its next generation multi-mission microsatellite "Triton-X" to enable affordable satellite applications in LEO. The consideration of a single-frequency receiver is especially interesting for Triton-X as it uses a 12-channel L1 receiver. Although Triton-X onboard GNSS receiver leverages only GPS signals, the proposed navigation scheme can be used with other GNSS receivers.

Triton-X being a multi-mission platform, the mission to which this algorithm is to be applied is tentative and the estimation and control requirements are not yet concrete, however, the estimation scheme was developed with two main requirements in mind,

1. The complexity of the algorithms has to be bearable by the Triton-X onboard computer (OBC).
2. The algorithm is to be implemented for missions which do not require stringent onboard estimation accuracy such as inspection and gravimetry missions D'Errico (2012).

The first requirement constrains the tweaks that could be done to the already existing algorithms in the literature. For instance, double-difference integer ambiguity resolution routines are excluded from the proposed scheme since it would be a computational burden on the OBC, in spite of the fact that these techniques are expected to improve the estimation accuracy while compromising the convergence time.

To be more concrete about the second requirement, it is assumed that an estimation error of less than 0.5 m (3D RMS) is required, which is similar to the real-time orbit determination requirements of the PRISMA technology demonstration mission De Florio & D'Amico (2010). Indeed, for large inter-satellite distances with loose relative navigation requirements, differencing the onboard available position solution is shown in Tancredi et al. (2015) to be a good alternative to differencing the GNSS observables, although with reference to dual frequency receivers. Differencing the standalone onboard solutions for the adopted single-frequency receiver is not an option since the adopted receiver provides a position accuracy (1σ) of around 10 m Luxspace (2021), which shall provide estimates that are not compliant with the aforementioned requirements if the onboard position solutions are to be differenced. The exact make of the adopted GNSS receiver is hidden for commercial reasons.

2. Estimation strategy

The relative state estimation is considered between two spacecraft, a target and a chaser. The two spacecraft are separated by a large distance and are equipped with single-frequency GNSS receivers. An intersatellite link from the target to the chaser is assumed to be constructed, which allows the transfer of the necessary data to estimate the position and velocity of the chaser with respect to the target. The treatment of latency and synchronization is out of the scope of this paper, nevertheless, interested reader is referred to Tancredi et al. (2014); Peng et al. (2019, 2021). It is important to note that although only two spacecraft are considered, the state estimation scheme proposed by this paper is applicable to any two spacecraft in a big formation. An Extended Kalman Filter (EKF) Jazwinski (1970) is proposed to process the GNSS data in order to provide relative position and velocity estimates that are inline with the mission requirements discussed in **Section 1**. Indeed, using and EKF for relative navigation is a common practice in the literature, however, a consensus has not been reached on the choice of the states to be estimated as well as the choice of the measurements to process. Different settings of the filter could lead to drastically different results even if the same data is processed Mahfouz et al. (2022). In this paper, the setup of the filter is sought to be optimized for the problem in hand.

2.1. Measurement choice

To achieve the relative navigation goal, the native GNSS measurements (i.e. the pseudo-range and the carrier phase) can be processed, while different advantages can arise from processing different linear combinations of these measurements. The use of the single, or double, difference of the native measurements or their combinations could also be useful Leick

et al. (2015).

For the problem in hand, a brief discussion of the possible measurements and their combinations is given in our preliminary study Mahfouz et al. (2022). It was concluded that the use of the Single Difference Carrier Phase (SDCP) BUSSE et al. (2003), the Single Difference GRoup And PHase Ionospheric Correction (GRAPHIC) Yunck (1993) combination (SDGR), as well as the Single Difference Geometry Free combination (SDGF) De Bakker et al. (2009) have potential to overcome the ionospheric effect, to the level that makes the resulting relative position and velocity estimates inline with the constraints of our problem. In the following discussion, the SDCP, the SDGR, and the SDGF combinations are modeled, and a brief reasoning is given as to why these specific combinations are chosen to be processed.

The SDCP is modelled as follows,

$$\rho_{sdcp} \coloneqq \rho_{cp}\big|_c - \rho_{cp}\big|_t = \Delta\rho + c\Delta\delta t + \lambda_f \Delta N - \Delta I + \Delta\eta + \nu_{sdcp}, \quad (1)$$

where ρ_{cp} is the carrier phase measurement, the subscripts $(\cdot)_c$ and $(\cdot)_t$ signify chaser-related and target-related quantities respectively with $\Delta(\cdot) = (\cdot)_c - (\cdot)_t$, ρ is the geometric range, c is the speed of light, δt is the receiver's clock bias from the GNSS time, λ_f is the wavelength corresponding to frequency f, N is the floating point ambiguity in cycles, I is the frequency dependent ionospheric delay, η is the additional distance between satellite and receiver antennas that the signal travels due to the rotation of the earth, and $\nu_{sdcp} \sim \mathcal{N}\left(0, \sigma^2_{sdcp}\right)$ is the SDCP noise, with $\mathcal{N}(\mu, \sigma^2)$ being the normal distribution with a mean μ and a variance σ^2 and $\sigma_{sdcp} \approx \sqrt{2}\sigma_{cp}$ where σ_{cp} is the standard deviation of the carrier phase measurement noise.

Letting $\boldsymbol{\omega}_e \approx \begin{bmatrix} 0 & 0 & \omega_e \end{bmatrix}^\intercal$ be the rotational velocity vector of the Earth in the Earth-Centered-Earth-Fixed (ECEF) frame, $\boldsymbol{r} = \begin{bmatrix} x & y & z \end{bmatrix}^\intercal$ be the position vector of the receiver of interest at the time of receiving the signal in the ECEF frame, and $\boldsymbol{r}^i = \begin{bmatrix} x^i & y^i & z^i \end{bmatrix}^\intercal$ be the position vector the GNSS satellite i at the time of transmitting the signal, also represented in the ECEF frame, the correction distance η can be written as follows Leick et al. (2015),

$$\eta = \frac{\omega_e}{c}\left(x^i y - x y^i\right). \quad (2)$$

Similar to the SDCP, the SDGR as well as the SDGF are modeled as,

$$\rho_{sdgr} \coloneqq \frac{1}{2}\left(\rho_{pr} + \rho_{cp}\right)_c - \frac{1}{2}\left(\rho_{pr} + \rho_{cp}\right)_t = \Delta\rho + c\Delta\delta t + \frac{1}{2}\lambda_f \Delta N + \Delta\eta + \nu_{sdgr}, \quad (3)$$

$$\rho_{sdgf} \coloneqq \left(\rho_{pr} - \rho_{cp}\right)_c - \left(\rho_{pr} - \rho_{cp}\right)_t = 2\Delta I - \lambda_f \Delta N + \nu_{sdgf}, \quad (4)$$

where ρ_{pr} is the pseudorange measurement, and $\nu_{sdgr} \sim \mathcal{N}\left(0, \sigma^2_{sdgr}\right)$ and $\nu_{sdgf} \sim \mathcal{N}\left(0, \sigma^2_{sdgf}\right)$ are the noises corresponding to the SDGR and the SDGF respectively, with $\sigma_{sdgr} \approx \sigma_{pr}/\sqrt{2}$ and $\sigma_{sdgr} \approx \sqrt{2}\sigma_{pr}$, where σ_{pr} is the standard deviation of the pseudorange measurement noise.

A general signal that travels from a GNSS satellite to a receiver experiences a non-dispersive tropospheric delay, a dispersive multipath delay, as well as satellite and receiver instrumental delays. The tropospheric and the multipath effects are omitted as the receivers in the context of this paper fly above the troposphere and are far away from any reflecting surface. The receiver's instrumental delays are assimilated to the clock bias of the reciever, while the satellite's instrumental delays are nullified in the single difference quantities (i.e. SDCP, SDGR, and SDGF).

Having chosen the observables to be processed by the EKF, the measurement vector $\boldsymbol{z}$ of the EKF is constructed as,

$$\boldsymbol{z} \coloneqq \begin{bmatrix} \boldsymbol{\rho}_{sdcp} \\ \boldsymbol{\rho}_{sdgr} \\ \boldsymbol{\rho}_{sdgf} \end{bmatrix}. \quad (5)$$

It is to be noted that $\boldsymbol{\rho}_{sdcp}$, $\boldsymbol{\rho}_{sdgr}$, and $\boldsymbol{\rho}_{sdgf}$ are not scalar values that correspond to one GNSS satellite, but rather vectors that comprise the measured combinations from all the commonly tracked satellites. In this setting, the length of the measurement vector is $3n$, where n is the number of channels of the GNSS receiver (12 channels for the Triton-X onboard receiver).

The choice for the measurements to be staged for processing in our context is justified in the following points,

1. The relative position and velocity of one spacecraft with respect to another are estimated directly by the filter, instead of estimating the absolute states of the two spacecraft then subtract the state vector of one spacecraft from that of the other. In this setting, differential measurements have to be used, hence the single difference combinations are chosen. Moreover, another advantage of differential measurements is that they allow some of the common biases (i.e. satellite's clock bias and instrumental delays) to cancel out.
2. As the ionospheric delay is the most significant bias to be accounted for, the use of ionospheric-free combinations comes as no surprise. That is why the SDGR is used, as GRAPHIC is the only known single-frequency ionospheric-free combination.
3. Although the SDGR is an ionospheric-free combination, it is still a noisy measurement, that is why more precise combinations, like the SDCP, need to be included to augment the overall accuracy of the filter. It has to be noted that the inclusion of the SDCP comes with its own challenges, like having to estimate the ionospheric effect as well as the float ambiguities.
4. It is believed that the inclusion of the ionospheric geometry-free combination, the SDGF, shall assist in estimating the ionospheric delay as well as the ambiguities however being coarse. This hypothesis was shown to be true in Mahfouz et al. (2022).
5. Despite the availability of range measurements directly from the intersatellite link, it is a coarse imprecise measurement Crisan et al. (2020), which is not expected to improve the overall estimation precision.

2.2. *Ionospheric model*

The ionospheric delay (I) which appears in the measurement models (1) and (4) is modeled as the integral of the linear electron density along the ray path between the satellite and receiver Klobuchar (1987) as follows,

$$I = \alpha(f)\, S, \tag{6}$$

where $\alpha(f)$ is the frequency dependant mapping function between the Slant Total Electron Content (STEC) and the signal delay and S is the STEC.

The mapping function $\alpha(f)$ is modeled by the following formula Rao (2008),

$$\alpha(f) = \frac{40.3 \cdot 10^{16}}{f^2}\ \text{m/TECU}, \tag{7}$$

where f is the carrier frequency in Hz, which for GPS L1 is equal to 1575.42 MHz, and TECU is the Total Electrol Content Unit (TECU = 10^{16} e^-/m^2). Furthermore, The slant total electron content (STEC) is itself modeled by the Linear Thin Shell (LTS) model Renga et al. (2018) as,

$$\begin{aligned} S &= M_{ts} V, \\ M_{ts} &= \frac{R_\oplus + h_{ts}}{r_u \sqrt{\left(\frac{R_\oplus + h_{ts}}{r_u}\right)^2 - \cos^2\left(E_u^i\right)}}, \\ V &= \begin{bmatrix} 1 & \delta\phi_{ipp} & \delta\lambda_{ipp} \end{bmatrix} \cdot \boldsymbol{q} \end{aligned} \tag{8}$$

where M_{ts} is the thin shell mapping function from the Vertical Total Electron Content (VTEC) to the Slant Total Electron Content (STEC) through the path of the ray, $R_\oplus$ is the mean radius of the Earth, h_{ts} is the altitude of the thin shell, r_u is the norm of user u (i.e. receiver u) position vector in an Earth centered reference frame, E_r^i is the elevation angle of the GNSS satellite i with respect to the user u measured up from the local horizon, and V is the Vertical Total Electron Content (VTEC). The bilinear approximation of the VTEC Komjathy & Langley (1996) is dependant on the coefficient vector $\boldsymbol{q} = \begin{bmatrix} q_0 & q_1 & q_2 \end{bmatrix}^\intercal$ which is to be estimated by the filter, as well as $\delta\phi_{ipp}$ and $\delta\lambda_{ipp}$ which are defined as follows,

$$\begin{aligned} \delta\phi_{ipp} &\coloneqq \phi_{ipp} - \phi_u, \\ \delta\lambda_{ipp} &\coloneqq \lambda_{ipp} - \lambda_u, \end{aligned} \tag{9}$$

where ϕ_{ipp} and λ_{ipp} are the latitude and longitude respectively of the Ionospheric Pierce Point (IPP) Centre National d'Études Spatiales et al. (2011), while ϕ_u and λ_u are those of the receiver. A common arbitrary choice for ground-based receivers is setting

h_{ts} as the altitude of the F2 peak, nonetheless, in this paper, it is set to a free variable that is estimated by the EKF.

Indeed, the ionospheric effect is the largest bias in the available measurements that needs to be accounted for, that is why the LTS model is chosen, as it is preferred to the other empirical ionospheric models such as the commonly used Lear mapping Lear (1988). It provides better estimates of the ionospheric delay with slightly higher computational demands Renga et al. (2018).

2.3. State variables choice

This section is dedicated to introducing the state variables to be estimated by the EKF. Clearly, the main variables that need to be estimated are the baseline vector and the relative velocity between two spacecraft, however, some auxiliary variables (e.g. receiver's clock bias, carrier phase float ambiguities,...) need to be estimated in order to increase the precision of the filter. In fact, if an EKF filter is run without considering these auxiliary variables, especially the receiver's clock bias, it is susceptible to generate unusable estimates.

As discussed in *Section 2.1*, a unique set of state variables does not exist, and the choice of the state vector is customary. In fact, the choice of the state variables to be estimated is heavily dependant on the choice of the measurements combinations to be fed to the filter, which itself is customary to choose. In this paper, the advantages of the SDCP, the SDGR, and the SDGF combinations, defined in equations (1), (3), and (4) respectively, are leveraged

The state vector $\boldsymbol{X}$ is constructed based on the chosen measurements. The choice of the state variables is presented below.

$$\boldsymbol{X} \coloneqq \begin{bmatrix} \Delta\boldsymbol{x}^\intercal & c\Delta\delta t & c\Delta\dot{\delta}t & h_{ts} & \boldsymbol{q}^\intercal & \Delta\boldsymbol{N}^\intercal \end{bmatrix}^\intercal, \tag{10}$$

where $\boldsymbol{x} \coloneqq \begin{bmatrix} \boldsymbol{r}^\intercal & \boldsymbol{v}^\intercal \end{bmatrix}^\intercal$ is the vector that contains the position and velocity coordinates of a receiver in the Earth-Centred, Earth-Fixed (ECEF) frame, $\Delta\delta t$ is the differential receiver's clock bias with $\Delta\dot{\delta}t$ being its rate of change, h_{ts} and $\boldsymbol{q}$ (a 3-element vector) are the parameters related to the ionospheric model, and $\boldsymbol{N}$ is the carrier phase float ambiguity vector for all the commonly tracked satellites. The length of the state vector in this setting is $12 + n$, where n is the number of channels of the GNSS receiver (12 channels for Triton-X onboard receiver).

3. Mathematical models

In this section, the nonlinear dynamical models of the state variables together with the Jacobian matrices necessary for the operation of the EKF are presented.

The dynamics of the state vector are separated into the orbital dynamics, concerning the $\Delta\boldsymbol{x}$ vector, and the dynamics of the auxiliary variables which concern the rest of the state variables in (10).

3.1. Orbital dynamics

The motion of a satellite that moves under the gravity field of the Earth can be formulated as a Perturbed Two-Body Problem (PTBP) in the ECEF frame by applying Transport theorem Rao (2006) on the PTBP equations of motion in an inertial frame as follows,

$$\ddot{\boldsymbol{r}} = -\frac{\mu_\oplus}{r^3}\boldsymbol{r} - \boldsymbol{\omega}_e \times \boldsymbol{v} - \boldsymbol{\omega}_e \times \boldsymbol{\omega}_e \times \boldsymbol{r} + \boldsymbol{a}_{ctrl} + \boldsymbol{a}_{J_2} + \boldsymbol{w}_{\boldsymbol{v}}, \tag{11}$$

where $\boldsymbol{r}$ is the position vector of the satellite, r is the magnitude of that position vector, $\mu_\oplus$ is the Earth's standard gravitational parameter, $\boldsymbol{a}_{ctrl}$ is the known input control vector, $\boldsymbol{a}_{J_2}$ is the J_2 perturbing acceleration vector modeled by (A.4) in **Appendix A**, and $\boldsymbol{w}_{\boldsymbol{v}}$ collates all the unmodeled disturbance accelerations. It is important to note that all the vectors in (11) are expressed in the ECEF frame, and that (11) is derived by approximating the rotation of the ECEF frame to be only around the z-axis of the ECI frame.

Equation (11) can be easily transformed to,

$$\dot{\boldsymbol{x}} \coloneqq \begin{bmatrix} \dot{\boldsymbol{r}} \\ \dot{\boldsymbol{v}} \end{bmatrix} = \begin{bmatrix} \boldsymbol{v} \\ -\frac{\mu_\oplus}{r^3}\boldsymbol{r} - 2\boldsymbol{\omega}_e \times \boldsymbol{v} - \boldsymbol{\omega}_e \times \boldsymbol{\omega}_e \times \boldsymbol{r} + \boldsymbol{a}_{ctrl} + \boldsymbol{a}_{J_2} + \boldsymbol{w}_{\boldsymbol{v}} \end{bmatrix}. \tag{12}$$

Using (12), the relative orbital dynamics between the chaser and the target spacecraft in the ECEF frame can be expressed as:

$$\Delta\dot{\boldsymbol{x}} \coloneqq \begin{bmatrix} \Delta\dot{\boldsymbol{r}} \\ \Delta\dot{\boldsymbol{v}} \end{bmatrix} = \begin{bmatrix} \Delta\boldsymbol{v} \\ \frac{\mu_\oplus}{r_t^3}\left(\boldsymbol{r}_t - \frac{r_t^3(\boldsymbol{r}_t+\Delta\boldsymbol{r})}{\left(r_t^2+2\boldsymbol{r}_t\cdot\Delta\boldsymbol{r}+\Delta r^2\right)^{3/2}}\right) + \Delta\boldsymbol{a}_{J_2} \\ -2\boldsymbol{\omega}_e \times \Delta\boldsymbol{v} - \boldsymbol{\omega}_e \times \boldsymbol{\omega}_e \times \Delta\boldsymbol{r} + \Delta\boldsymbol{a}_{ctrl} + \boldsymbol{w}_{\Delta\boldsymbol{v}} \end{bmatrix}, \tag{13}$$

where $\boldsymbol{r}_t$ is the position vector of the target satellite with a magnitude of r_t, $\Delta\boldsymbol{r} = \boldsymbol{r}_c - \boldsymbol{r}_t$ and $\Delta\boldsymbol{v} = \boldsymbol{v}_c - \boldsymbol{v}_t$ are the relative position and velocity vectors respectively from the target to the chaser spacecraft with magnitudes of Δr and Δv, all expressed in the ECEF frame. Moreover, $\Delta\boldsymbol{a}_{J_2}$ is the differential J_2 perturbation vector and $\boldsymbol{w}_{\Delta\boldsymbol{v}} \sim \mathcal{N}(0, \mathbb{Q}_{\Delta\boldsymbol{v}})$ collates all the relative acceleration noises.

Only the J_2 perturbation is modeled in this research as it is expected to have the greatest influence on the relative dynamics between the two largely separated spacecraft. Furthermore, $\mathbb{Q}_{\Delta\boldsymbol{v}}$ is defined as,

$$\mathbb{Q}_{\Delta\boldsymbol{v}} = \operatorname{diag}\begin{pmatrix}\sigma^2_{\Delta v_x} & \sigma^2_{\Delta v_y} & \sigma^2_{\Delta v_z}\end{pmatrix}. \tag{14}$$

In the prediction phase of the EKF, equation (13) is numerically integrated after omitting the disturbance, to obtain a prediction of the relative position and velocity states at each time step. It is important to note that an estimate of the absolute position and velocity vectors of the target spacecraft is essential for the numerical integration of (13) and for a proper operation of the EKF. These are directly acquired from the receiver's noisy onboard solution at each prediction step. The same approach was used in Tancredi et al. (2014).

3.2. Dynamics of the auxiliary variables

The state variables $c\Delta\dot{\delta}t$ and $\boldsymbol{q}$ are modeled as Gaussian random walk processes while the rest of the auxiliary variables are modeled as constants,

$$\begin{aligned} c\Delta\ddot{\delta}t &= w_{c\Delta\dot{\delta}t}, \\ \dot{h}_{ts} &= 0, \\ \dot{\boldsymbol{q}} &= \boldsymbol{w}_{\boldsymbol{q}}, \\ \Delta\dot{\boldsymbol{N}}_{CP} &= \boldsymbol{0}, \end{aligned} \tag{15}$$

where $w_{c\Delta\dot{\delta}t} \sim \mathcal{N}\left(0, \sigma^2_{c\Delta\dot{\delta}t}\right)$ and $\boldsymbol{w}_{\boldsymbol{q}} \sim \mathcal{N}\left(0, \mathbb{Q}_{\boldsymbol{q}}\right)$. The noise in the $c\Delta\ddot{\delta}t$ signal is set to account for the sudden clock jumps that manufacturers embed into their receivers in order to control the magnitude of the clock biases Guo & Zhang (2012). Moreover, $\mathbb{Q}_{\boldsymbol{q}}$ is defined as,

$$\mathbb{Q}_{\boldsymbol{q}} = \operatorname{diag}\begin{pmatrix}\sigma^2_{q_0} & \sigma^2_{q_1} & \sigma^2_{q_2}\end{pmatrix}. \tag{16}$$

3.3. State transition matrix

With the definition of the state variables (10) in mind, together with their models (13) and (15), the State Transition Matrix (STM) which is essential for the operation of the EKF can be divided into several sub-matrices as,

$$\mathbb{F} := \frac{\partial \boldsymbol{X}_k}{\partial \boldsymbol{X}_{k-1}} = \begin{bmatrix} \mathbb{F}_{\Delta\boldsymbol{x}} & \boldsymbol{0} & \boldsymbol{0} & \boldsymbol{0} & \mathbb{0} & \mathbb{0} \\ \boldsymbol{0}^\intercal & 1 & t_k - t_{k-1} & 0 & \boldsymbol{0}^\intercal & \boldsymbol{0}^\intercal \\ \boldsymbol{0}^\intercal & 0 & F_{c\Delta\dot{\delta}t} & 0 & \boldsymbol{0}^\intercal & \boldsymbol{0}^\intercal \\ \boldsymbol{0}^\intercal & 0 & 0 & F_{h_{ts}} & \boldsymbol{0}^\intercal & \boldsymbol{0}^\intercal \\ \mathbb{0} & \boldsymbol{0} & \boldsymbol{0} & \boldsymbol{0} & \mathbb{F}_{\boldsymbol{q}} & \mathbb{0} \\ \mathbb{0} & \boldsymbol{0} & \boldsymbol{0} & \boldsymbol{0} & \mathbb{0} & \mathbb{F}_{\Delta\boldsymbol{N}} \end{bmatrix}, \tag{17}$$

where $\mathbb{F}_{\Delta\boldsymbol{x}}$, $F_{c\Delta\dot{\delta}t}$, $F_{h_{ts}}$, $\mathbb{F}_{\boldsymbol{q}}$, and $\mathbb{F}_{\Delta\boldsymbol{N}}$ are the state transition matrices for $\Delta\boldsymbol{x}$, $c\Delta\dot{\delta}t$, h_{ts}, $\boldsymbol{q}$, and $\Delta\boldsymbol{N}$ respectively, while t_k and t_{k-1} are two consecutive time instants to which the STMs correspond. Furthermore, $\boldsymbol{0}$ represents a vector of zeros and $\mathbb{0}$ is a matrix of zeros.

Various linearization techniques can be adopted in order to obtain the STM $\mathbb{F}_{\Delta\boldsymbol{x}}$ Carter (1998), nonetheless, it is not used to propagate the states, but rather to propagate the estimated states variance-covariance matrix (refer to the prediction phase of the EKF Jazwinski (1970)), hence the constraint of having a very precise STM becomes much looser. The simple STM obtained from the closed form solution to the Clohessy–Wiltshire (CW) equations Clohessy & Wiltshire (1960) can also be used, however, one needs to keep an eye on the fact that CW equations provide the solution in Hill's frame of the target spacecraft, and the obtained STM has to be rotated to the ECEF. In this paper, an even simpler approach is adopted by linearizing the equations of motion (13) taking the target's orbit as a reference for the linearization. In this case, the STM of the relative states $\mathbb{F}_{\Delta\boldsymbol{x}}$ is only dependent on the target's states as suggested by (B.3). **Appendix B** includes the details of why this assumption is plausible. Approximating the Jacobian of the relative states by the

Jacobian of the target's states yields,

$$\begin{aligned}\mathbb{J}_{\Delta \boldsymbol{x}} &\coloneqq \frac{\partial \Delta \dot{\boldsymbol{x}}}{\partial \Delta \boldsymbol{x}} \approx \left.\frac{\partial \dot{\boldsymbol{x}}}{\partial \boldsymbol{x}}\right|_{\boldsymbol{x}=\boldsymbol{x}_t} \\ \mathbb{F}_{\Delta \boldsymbol{x}} &\coloneqq \frac{\partial \Delta \boldsymbol{x}_k}{\partial \Delta \boldsymbol{x}_{k-1}} \approx \exp\left((t_k - t_{k-1})\, \mathbb{J}_{\Delta \boldsymbol{x}}|_{\boldsymbol{x}_t|_{k-1}}\right),\end{aligned} \tag{18}$$

where $\mathbb{J}_{\Delta \boldsymbol{x}}$ is the state-dependant Jacobian matrix that can be calculated by partial differentiation of (12), while $\mathbb{J}_{\Delta \boldsymbol{x}}|_{\boldsymbol{x}_t|_{k-1}}$ is the same matrix evaluated at the target's state at time t_{k-1}.

The state transition matrices of the auxiliary variables can be directly derived from the linear system of equations (15) after omitting the noise as follows,

$$\begin{aligned} &F_{c\Delta\dot{\delta}t} = 1, \\ &F_{h_{ts}} = 1, \\ &\mathbb{F}_{\boldsymbol{q}} = \mathbb{I}_3. \\ &F_{\Delta \boldsymbol{N}}|_{i,j} = \begin{cases} 1, & P_i \in \mathcal{P}_{k-1} \;\&\; i = C_i|_k \;\&\; j = C_i|_{k-1} \\ 0, & \text{Otherwise} \end{cases}, \end{aligned} \tag{19}$$

where $\mathbb{I}_{(\cdot)}$ is an identity matrix of size $(\cdot)$, $F_{\Delta \boldsymbol{N}}|_{i,j}$ is the entry $(i,\ j)$ of the $\mathbb{F}_{\Delta \boldsymbol{N}}$ matrix, P_i is the PseudoRandom Noise (PRN) code of the i^{th} commonly tracked satellite (at time t_k), $\mathcal{P}_{k-1}$ is the set of PRNs of the commonly visible satellites at time instant t_{k-1}, and $C_i|_k$ and $C_i|_{k-1}$ are indices to the target's receiver channels that captured the measurement from the i^{th} commonly visible satellite at times t_k and t_{k-1} respectively. Indeed, the differential ambiguity for the newly tracked satellites are set to zero, however, the process noise variance-covariance matrix has to be adapted to reflect the uncertainty of this initial guess. Equation (19) can not only be used to construct the full STM (17), but also to propagate the auxiliary states in the prediction phase of the EKF.

3.4. Measurement model

Although the measurement vector in (5) is modeled by equations (1), (3), and (4), the Jacobian matrix $\mathbb{H}$ of these nonlinear functions needs to be constructed as a requirement for the update phase of the EKF. Concretely, the nonlinear measurement model is presented once again as follows,

$$\boldsymbol{h} = \begin{bmatrix} \Delta\boldsymbol{\rho} + c\Delta\delta t + \lambda_f \Delta \boldsymbol{N} - \alpha(f)\,\Delta \boldsymbol{S} + \Delta\boldsymbol{\eta} \\ \Delta\boldsymbol{\rho} + c\Delta\delta t + \frac{1}{2}\lambda_f \Delta \boldsymbol{N} + \Delta\boldsymbol{\eta} \\ 2\alpha(f)\,\Delta \boldsymbol{S} - \lambda_f \Delta \boldsymbol{N} \end{bmatrix}. \tag{20}$$

where the differential STEC vector $\Delta \boldsymbol{S}$ is obtained from the VTEC vector according to the mapping (8).

The state dependant Jacobian matrix $\mathbb{H}$ can then be obtained,

$$\mathbb{H} \coloneqq \frac{\partial \boldsymbol{h}}{\partial \boldsymbol{X}} = \begin{bmatrix} \mathbb{H}_{\Delta \boldsymbol{r}} & \mathbb{0} & \mathbf{1} & \mathbf{0} & -\boldsymbol{H}_{h_{ts}} & -\mathbb{H}_{\boldsymbol{q}} & \lambda_f \mathbb{H}_{\Delta \boldsymbol{N}} \\ \mathbb{H}_{\Delta \boldsymbol{r}} & \mathbb{0} & \mathbf{1} & \mathbf{0} & \mathbf{0} & \mathbb{0} & \frac{\lambda_f}{2}\mathbb{H}_{\Delta \boldsymbol{N}} \\ \mathbb{0} & \mathbb{0} & \mathbf{0} & \mathbf{0} & 2\boldsymbol{H}_{h_{ts}} & 2\mathbb{H}_{\boldsymbol{q}} & -\lambda_f \mathbb{H}_{\Delta \boldsymbol{N}} \end{bmatrix}, \tag{21}$$

where $\mathbb{H}_{\Delta \boldsymbol{r}}$, $\boldsymbol{H}_{h_{ts}}$, $\mathbb{H}_{\boldsymbol{q}}$, and $\mathbb{H}_{\Delta \boldsymbol{N}}$ are partial derivative matrices that have the dimensions of $m \times 3$, $m \times 1$, $m \times 3$, and $m \times n$ respectively, with m being the number of the commonly visible satellites and n is the number of channels of the receiver.

Matrix $\mathbb{H}_{\Delta \boldsymbol{r}}$ is a Jacobian matrix that can be obtained by partial differentiation of the $(\Delta\boldsymbol{\rho} + \Delta\boldsymbol{\eta})$ part of the measurement model (20) using the states of the target,

$$\begin{aligned}\mathbb{H}_{\Delta \boldsymbol{r}} \coloneqq \frac{\partial}{\partial \Delta \boldsymbol{r}}(\Delta\boldsymbol{\rho} + \Delta\boldsymbol{\eta}) \approx \left.\frac{\partial}{\partial \boldsymbol{r}}(\boldsymbol{\rho} + \boldsymbol{\eta})\right|_t = \\ \begin{bmatrix} \boldsymbol{e}_t^1 & \boldsymbol{e}_t^2 & \dots & \boldsymbol{e}_t^m & \mathbf{0} & \dots & \mathbf{0} \end{bmatrix}^{\mathsf{T}},\end{aligned} \tag{22}$$

where the zero vectors at the end account for the target's receiver channels that did not track any satellite or that tracked a satellite that is not visible by the chaser, $\boldsymbol{e}_t^i$ comprises the unit baseline vector from the i^{th} commonly tracked satellite to the target in the ECEF frame in addition to a correction term for the Earth's rotation,

$$\boldsymbol{e}_t^i = \frac{\boldsymbol{r}_t - \boldsymbol{r}^i}{\left\|\boldsymbol{r}_t - \boldsymbol{r}^i\right\|} + \frac{\omega_e}{c}\begin{bmatrix} -y^i & x^i & 0 \end{bmatrix}^{\mathsf{T}}. \tag{23}$$

Using (6), (7), and (8), the i^{th} entry in the $\boldsymbol{H}_{h_{ts}}$ vector, which corresponds to the measurement from the i^{th} commonly visible satellite by both the chaser and the target, can be written as,

$$\begin{aligned} H_{h_{ts}}\big|_i &= \frac{40.3 \cdot 10^{16}}{f^2}\left[\left(\frac{\partial M_{ts}}{\partial h_{ts}} V\right)_c^i - \left(\frac{\partial M_{ts}}{\partial h_{ts}} V\right)_t^i\right], \\ \frac{\partial M_{ts}}{\partial h_{ts}} &= -\frac{\cos^2\left(E_u^i\right)}{r_u \sqrt{\left[\left(\frac{R_\oplus + \mathrm{h_{ts}}}{r_u}\right)^2 - \cos^2\left(E_u^i\right)\right]^3}}, \end{aligned} \tag{24}$$

while the i^{th} row in the $\mathbb{H}_{\boldsymbol{q}}$ can be written as,

$$\begin{aligned} H_{\boldsymbol{q}}\big|_i &= \frac{40.3 \cdot 10^{16}}{f^2}\left[\left(M_{ts}\frac{\partial V}{\partial \boldsymbol{q}}\right)_c^i - \left(M_{ts}\frac{\partial V}{\partial \boldsymbol{q}}\right)_t^i\right], \\ \frac{\partial V}{\partial \boldsymbol{q}} &= \begin{bmatrix} 1 & \delta\phi_{ipp} & \delta\lambda_{ipp} \end{bmatrix}. \end{aligned} \tag{25}$$

Matrix $\mathbb{H}_{\Delta \boldsymbol{N}}$ is, in fact, a boolean rearrangement matrix with entries,

$$H_{\Delta \boldsymbol{N}}|_{i,j} = \begin{cases} 1, & P_i \in \mathcal{P}_{k-1} \ \& \ j = C_i \\ 0, & \text{Otherwise} \end{cases}. \tag{26}$$

4. EKF initialization and operation

In order for the EKF to operate properly, it needs an initial guess for the state vector ($\boldsymbol{X}$) as well as the estimated states variance-covariance matrix ($\mathbb{P}$). Indeed, many ways such as the available onboard solution of each satellite or weighted least-square schemes can be incorporated to calculate a fairly close initial relative position and velocity vectors, yet, in order to demonstrate that the proposed filter converges even for uncertain initial conditions, the state variables are initiated with randomly selected values within the true range of each variable. The estimation covariance matrix, on the other hand, is inaugurated as a diagonal matrix with large variances to reflect the uncertainties of the initial guess of the state vector. During operation, it is of a huge importance to re-initiate the values of $\Delta \boldsymbol{N}$ to account for newly tracked satellites (see equation (19)). Once a value is initialized, the corresponding process noise variance needs to be set to a large value in the process noise variance-covariance matrix $\mathbb{Q}$. Moreover, a proper rearrangement of the estimated state variance-covariance matrix ($\mathbb{P}$) needs to be carried out in order to account for the satellites that went out of sight.

Besides the initialization of the state vector and the estimated states variance-covariance matrix, two other variance-covariance matrices need to be defined for the EKF to operate efficiently, the process noise variance-covariance matrix $\mathbb{Q}$ and the observation variance-covariance matrix $\mathbb{R}$.

The process noise variance-covariance matrix $\mathbb{Q}$ is set to the following semi-definite time-varying matrix,

$$\mathbb{Q} = \text{diag}\left(\mathbb{0}, \quad \mathbb{Q}_{\Delta \boldsymbol{v}}, \quad 0, \quad \sigma^2_{c\Delta\delta t}, \quad 0, \quad \mathbb{Q}_{\boldsymbol{q}}, \quad \mathbb{Q}_{\Delta \boldsymbol{N}}\right), \tag{27}$$

where $\mathbb{Q}_{\Delta \boldsymbol{N}}$ is generally a matrix of zeros, except when a newly tracked satellite is introduced, then the corresponding diagonal entry is set to a large value to reflect the unreliability of the corresponding initiated ΔN value. The state variables' noises are assumed uncorrelated, thus all the covariance elements of the $\mathbb{Q}$ matrix are zero. Furthermore, the process noise variance-covariance matrix is in general a time-varying matrix, as $\mathbb{Q}_{\Delta \boldsymbol{N}}$ need constant rearrangement as new satellites are being tracked. The diagonal entries for $\mathbb{Q}_{\Delta \boldsymbol{N}}$ are defined as,

$$Q_{\Delta \boldsymbol{N}}|_{i,i} \coloneqq \begin{cases} 10^2, & C_i \text{ tracks a new satellite} \\ 0, & \text{Otherwise} \end{cases}, \tag{28}$$

Although the multipath effect was not incorporated in the measurements model (20), it is not entirely true that a receiver in a low Earth orbit will not experience any multipath interference. It has been shown in Ceva & Parkinson (1993) that the Earth's surface reflections could indeed disturb the GNSS signals especially those which have to travel from a low elevation satellite with respect to the receiver. Nonetheless, this type of interference lasts only for short periods and can be avoided by choosing a suitable cut-off elevation angle, beyond which the signal is simply discarded. Instead of hard coding a cut-off elevation angle, which also means that parts of the observations have to be discarded, the measurement variance-covariance matrix is set to vary with the elevation angle of the transmitting satellite. In this setting, the lower the elevation angle, the higher the variance of the observation noise is set.

Assuming uncorrelated measurement noises, the observation noise variance-covariance matrix is set to the following time-varying matrix,

$$\mathbb{R} = \begin{bmatrix} \mathbb{R}_{sdcp} & \mathbb{0} & \mathbb{0} \\ \mathbb{0} & \mathbb{R}_{sdgr} & \mathbb{0} \\ \mathbb{0} & \mathbb{0} & \mathbb{R}_{sdgf} \end{bmatrix}, \tag{29}$$

where $\mathbb{R}_{sdcp}$, $\mathbb{R}_{sdgr}$, and $\mathbb{R}_{sdgf}$ are the noise variance-covariance matrices corresponding to the SDCP, SDGR, SDGF measurements respectively. The off-diagonal elements of the $\mathbb{R}_{sdcp}$, $\mathbb{R}_{sdgr}$, and $\mathbb{R}_{sdgf}$ matrices are all zeros, while the diagonal elements are defined as,

$$R_{(\cdot)}\big|_{i,i} \coloneqq \frac{\sigma^2_{(\cdot)}}{\sin^2\left(E^i_{min}\right) + \epsilon}, \tag{30}$$

where $\sigma_{(\cdot)}$ is a predefined constant standard deviation for the observation (either the SDCP, the SDGR, or the SDGF),

$E^i_{min} := \min\left(\left|E^i_c\right|, \left|E^i_t\right|\right)$ is the minimum magnitude elevation angle between either the chaser or the target when both track the GNSS satellite (i), and ϵ is a small constant that acts as a safeguard from dividing by zero. Clearly, the size of each of the observation noise variance-covariance matrices is time-varying as it depends on the number of commonly tracked satellites.

During the operation of the EKF, a measurement vector at any time step is said to have at least one outlier in case the collective squared Mahalanobis distance Izenman (2008) is found to be greater than the inverse of the χ^2 cumulative distribution function of a significance level of 5% and with the length of the measurement vector as the degrees of freedom. Once a batch of measurements is detected to have outliers, those are detected and rejected using the individual squared Mahalanobis distance test Lopez (2017).

5. Results and discussion

In order to validate the algorithm, data from the SWARM mission European Space Agency (2022) are collected and simulated in a real-time setting. SWARM is an Earth observation mission that consists of three identical satellites, Alpha, Bravo, and Charlie; which were launched in November 2013.

The algorithm was tested on two different full days worth of the SWARM mission GNSS data, namely on 16-Jul-2014 and on 08-Dec-2020. These two days are chosen keeping in mind that the algorithm needs to be tested in best and the worst ionospheric conditions. The year 2020 witnessed the lowest solar activity of the SC24 solar cycle, hence, the best ionospheric conditions for GNSS navigation are expected. On the other hand, the peak of the SC24 solar cycle happened in 2014 and the worst ionospheric conditions are present around this time. Indeed, SC24 is not the most intense cycle in terms of the solar radiation, and consequently in the total electron content of the ionosphere. However, the authors did not manage to get access to other GNSS data that were recorded during a stronger solar cycle, for two receivers flying in low earth orbit with a large intersatellite distance.

The relative navigation is performed between Alpha (chaser) and Charlie (target) spacecraft which share the same orbit (150 km apart in 2014 and 100 km apart in 2020 on the dates of estimation).

In order for the EKF to operate efficiently, precise statistics of the process noises as well as the measurement noises need to be provided. A particular issue that needs to be addressed here is that, although the SDCP is usually considered a smooth signal with a noise level of order of millimeters, it cannot be considered very smooth in the context of largly separated receivers since the differential ionospheric delay is not negligible, and also as the ionospheric model is not accurate to the millimeters level. The statistics that were adopted in the simulations are presented in the Table 1. It is to be noted that the standard deviations of the noises of SDCP, SDGR, and SDGF can be deduced from the standard deviations of the carrier phase and the pseudorange noises (refer to the discussion in *Section 2.1*). Moreover, the standard deviation of the carrier phase noise for the 2014 data is set to a higher value than that of the 2020 data since the quality of the latter is better than that of the former.

Quantity	Value	Quantity	Value
$\sigma_{\Delta v_x} \equiv \sigma_{\Delta v_y} \equiv \sigma_{\Delta v_z}$	0.01 m/s^2	σ_{pr}	1.5 m
$\sigma_{c\dot{\Delta}\delta t}$	1 m/s	$\sigma_{cp}\big\vert_{2014}$	0.2 m
$\sigma_{q_0} \equiv \sigma_{q_1} \equiv \sigma_{q_2}$	$1/\sqrt{2}$ TECU/s	$\sigma_{cp}\big\vert_{2020}$	0.1 m

Table 1: Assumed constant statistics used in the simulations

After processing the 2014 data, estimates for the relative position and velocity vectors became available. Fig. 1 depicts the relative position errors, while Fig. 2 shows the relative velocity errors between the two spacecraft for the 2014 data. It is important to note that the relative position and velocity vectors are both estimated in the ECEF frame, then the error vectors as well as the estimation variance-covariance matrix are rotated to the Hill's frame of the target, by making use of the knowledge of the receiver's onboard solution for the target absolute position.

In order to obtain the error signals, the output of the

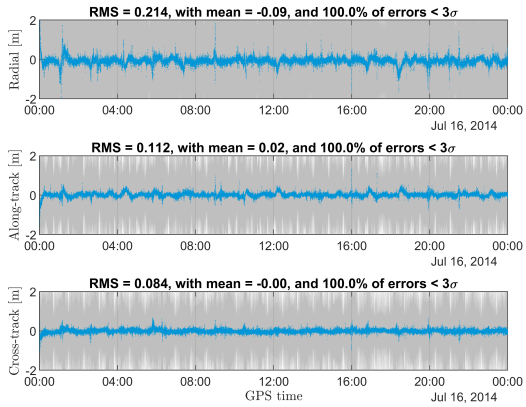

Fig. 1: Relative position error for 1 day of the SWARM mission data during the peak of SC24

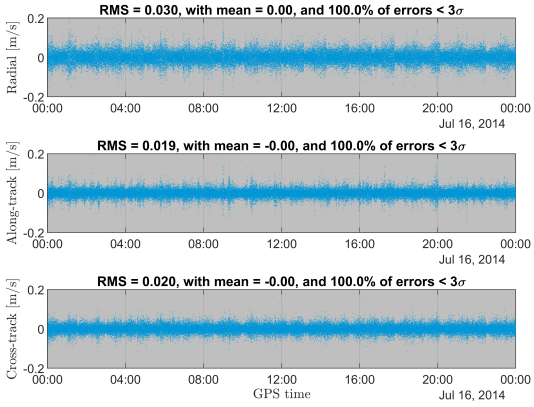

Fig. 2: Relative velocity error for 1 day of the SWARM mission data during the peak of SC24

post-processing Precise Orbit Determination (POD) algorithms is used as the ground truth. The POD output is accurate to the level of ±1 cm and is provided as part of the SWARM mission data.

For the 2014 data, 3D Root Mean Square (RMS) errors of 26 cm and 4 cm/s could be obtained for relative distance and relative speed respectively, while the filter converged after only 1 iteration. The convergence point in this setting is defined as the first occurrence of three consecutive filter estimation errors that are less than or equal to twice the RMS. Results in Figures 1 and 2 show that more than 99.7% of the errors lie below the 3σ threshold, with σ being the standard deviation of the estimation error, which suggests that our assumptions for the model and measurement statistics (see Table 1) are conservative.

Results with such convergence rate and accuracy, especially without implementing integer ambiguity resolution and fixing techniques, could only be obtained thanks to the incorporation of the presented measurement setting as well as the incorporation of a precise ionospheric model. This claim is supported by the preliminary trials to run the filter with different measurement and ionospheric model settings Mahfouz et al. (2022).

The number of the commonly tracked satellites as well as the Relative Position Dilution Of Precision (RP-DOP) for the 2014 data are depicted in Fig. 3, where the RP-DOP is defined as,

$$\text{RP-DOP} = \sqrt{\sigma^2_{\Delta x} + \sigma^2_{\Delta y} + \sigma^2_{\Delta z}}, \tag{31}$$

with $\sigma^2_{\Delta x}$, $\sigma^2_{\Delta y}$, and $\sigma^2_{\Delta z}$ being the estimation variances of the relative position components, extracted from the estimated variance-covariance matrix.

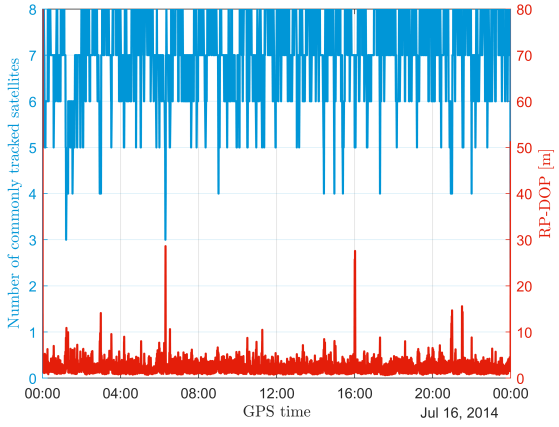

Fig. 3: Precision indicators

It is clear from Fig. 3 that the RP-DOP is likely to have spikes when the number of the commonly tracked satellites is low (e.g. 3 satellites). It is believed that these spikes appear not only due to the low number of the commonly visible satellites, but also due to the geometry of these tracked satellites as well as the elevation angles of the satellites with respect to the receivers (see for example the spike around 16:00 in Fig. 3 which appear when the number of commonly tracked satellite is fairly large, 5 satellites).

The 2020 data were as well processed and the relative position and velocity are estimated. Figures 4 and 5 illustrate the relative position and velocity estimation errors respectively for the 2020 data. An RMS error of 24 cm could be obtained

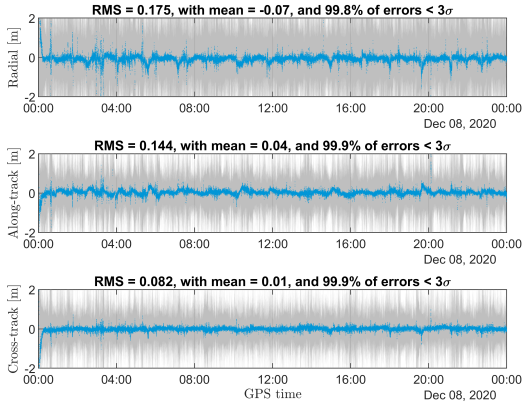

Fig. 4: Relative position error for 1 day of the SWARM mission data during the nadir of SC24

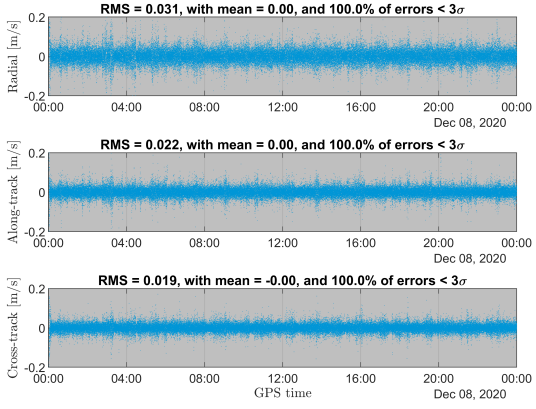

Fig. 5: Relative velocity error for 1 day of the SWARM mission data during the nadir of SC24

for the relative distance and of 4 cm/s for the relative speed. Indeed, the estimates of the 2020 data are of better quality than those of the 2014 data since the ionospheric conditions are better, however, the obtained estimation errors from both data are not substantially different. It is believed that thanks to the adoption of a fairly precise ionospheric model, almost indistinguishable performances of the filter could be obtained, even for different GNSS data streams with different ionospheric conditions.

6. Conclusion

In this paper, the problem of GNSS-based relative navigation between two spacecraft with large inter-satellite distance and with single-frequency receivers is treated through adopting the classical Extended Kalman Filter (EKF). Although using an EKF for relative navigation is a common practice in the literature, there exists endless variants of filter settings. The contribution of this research is the optimization of the filter setting for the specific problem in hand, by fixing the measurements to be fed to the filter, the handling of the ionospheric delay, the choice of the auxiliary state variables, and the definition of the process and measurement noises variance-covariance matrices.

A measurement setting comprising the Single Difference Carrier Phase (SDCP), the Single Difference GRAPHIC (SDGR), and the Single Difference Geometry Free (SDGF) combination is proposed. While the incorporation of the SDCP and the SDGR comes as no surprise, augmenting the measurement vector with the SDGF combination could help estimating the differential ionospheric delay as well as the differential floating point ambiguities, improving the overall estimation accuracy as well as the convergence time.

The fairly precise, however simple, thin shell ionospheric model was adopted as it provides superior estimates of the ionospheric delay than those of the commonly used empirical models.

As the quality of the GNSS signal improves proportionally with the elevation angle of the tracked satellite, the measurement noise variance-covariance matrix was made dependent on this elevation angle, which improved the reliability of the statistics of the measurement noises.

In order to test the sensitivity of the proposed filter setting to the change in ionospheric conditions, the algorithm was tested on a simulated real-time setting using two different data streams that were collected by the SWARM mission during the peak and the nadir of the SC24 solar cycle. Thanks to the adopted ionospheric model, the filter could produce almost indistinguishable relative position and velocity estimates for both cases. For the extreme ionospheric conditions during the peak of the solar cycle (in 2014), the filter could achieve 26 cm and 4 cm/s RMS errors in

the estimated relative distance and relative speed respectively, while it could achieve 24 cm and 4 cm/s RMS errors during the relaxed ionospheric conditions (in 2020).

It is important to emphasise that the obtained results could be achieved without implementing integer ambiguity resolution, which was excluded to relax the computational demand from the satellites onboard computer. Indeed, excluding the integer ambiguity resolution together with the adoption of an adequate ionospheric model contributed to the very fast convergence of the filter which typically converges after one iteration.

Acknowledgment

This work is supported by the Luxembourg National Research Fund (FNR) – AuFoSat project, BRIDGES/19/MS/14302465.

The experiments presented in this paper were carried out using the HPC facilities of the University of Luxembourg Varrette et al. (2014) – see hpc.uni.lu.

Appendix A. J_2 perturbation in the ECEF frame

The perturbing acceleration vector in the ECI frame resulting from the effect of the J_2 zonal harmonic can be modelled for a satellite with a position vector $\boldsymbol{r}^i = \begin{bmatrix} x^i & y^i & z^i \end{bmatrix}^\intercal$ (in the ECI) as,

$$\boldsymbol{a}^i_{J_2} = -\underbrace{\frac{3\mu_\oplus J_2 R_\oplus^2}{2r^7}}_{\psi} \underbrace{\begin{bmatrix} r^2-5z^2 & 0 & 0 \\ 0 & r^2-5z^2 & 0 \\ 0 & 0 & 3r^2-5z^2 \end{bmatrix}}_{\mathbb{M}} \begin{bmatrix} x^i \\ y^i \\ z^i \end{bmatrix}, \quad \text{(A.1)}$$

where J_2 the coefficient of the second zonal harmonic, $R_\oplus$ is the equatorial radius of the Earth, $r = \left\|\boldsymbol{r}^i\right\|$, and $z = z^i \approx z^e$, with $\boldsymbol{r}^e = \begin{bmatrix} x^e & y^e & z^e \end{bmatrix}^\intercal$ being the position vector of the satellite in the ECEF frame.

Ignoring the Earth's axial procession, vectors expressed in the ECI frame can be rotated to the ECEF frame as follows,

$$(\cdot)^e \approx \underbrace{\begin{bmatrix} \cos(\theta) & \sin(\theta) & 0 \\ -\sin(\theta) & \cos(\theta) & 0 \\ 0 & 0 & 1 \end{bmatrix}}_{\mathbb{A}} (\cdot)^i, \quad \text{(A.2)}$$

where θ is the Earth Rotation Angle (ERA).

Using (A.1) in conjunction with (A.2), the perturbing acceleration vector in the ECEF frame can be written as,

$$\boldsymbol{a}^e_{J_2} \approx -\psi \mathbb{A}\mathbb{M}\mathbb{A}^\intercal \boldsymbol{r}^e. \quad \text{(A.3)}$$

Due to the structure of $\mathbb{A}$ and $\mathbb{M}$, the term $\mathbb{A}\mathbb{M}\mathbb{A}^\intercal$ reduces to $\mathbb{M}$, which results in,

$$\boldsymbol{a}^e_{J_2} \approx -\psi \mathbb{M} \boldsymbol{r}^e. \quad \text{(A.4)}$$

Appendix B. Linearization of a general difference function

Consider the general vector valued function $\boldsymbol{f}(\boldsymbol{x})$ and the following difference function,

$$\Delta\boldsymbol{f} = \boldsymbol{f}(\boldsymbol{x}) - \boldsymbol{f}(\boldsymbol{x}_0). \quad \text{(B.1)}$$

The differential vector valued function $\Delta\boldsymbol{f}$ can be approximated by Taylor expansion around $\boldsymbol{x}_0$. Taking into account that $\Delta\boldsymbol{x} = \boldsymbol{x} - \boldsymbol{x}_0$, and ignoring the higher order terms, the Taylor approximation of $\Delta\boldsymbol{f}$ around $\boldsymbol{x}_0$ can be written as,

$$\Delta\boldsymbol{f} \approx \left(\boldsymbol{f}(\boldsymbol{x}_0) + \left.\frac{\partial \boldsymbol{f}}{\partial \boldsymbol{x}}\right|_{\boldsymbol{x}=\boldsymbol{x}_0} \Delta\boldsymbol{x}\right) - \boldsymbol{f}(\boldsymbol{x}_0) = \left.\frac{\partial \boldsymbol{f}}{\partial \boldsymbol{x}}\right|_{\boldsymbol{x}=\boldsymbol{x}_0} \Delta\boldsymbol{x}, \quad \text{(B.2)}$$

which suggests that,

$$\frac{\partial \Delta\boldsymbol{f}}{\partial \Delta\boldsymbol{x}} \approx \left.\frac{\partial \boldsymbol{f}}{\partial \boldsymbol{x}}\right|_{\boldsymbol{x}=\boldsymbol{x}_0}. \quad \text{(B.3)}$$

This approximation is valid as long as $\|\Delta\boldsymbol{x}\|$ is small in comparison to $\|\boldsymbol{x}_0\|$.

References

Ardaens, J.-S., & Gaias, G. (2018). Angles-only relative orbit determination in low earth orbit. *Advances in Space Research*, *61*(11), 2740–2760. URL: https://www.sciencedirect.com/science/article/pii/S0273117718302199. doi:https://doi.org/10.1016/j.asr.2018.03.016.

Ardaens, J.-S., & Gaias, G. (2019). A numerical approach to the problem of angles-only initial relative orbit determination in low earth orbit. *Advances in Space Research*, *63*(12), 3884–3899. URL: https://www.sciencedirect.com/science/article/pii/S0273117719301620. doi:https://doi.org/10.1016/j.asr.2019.03.001.

BUSSE, F. D., HOW, J. P., & SIMPSON, J. (2003). Demonstration of adaptive extended kalman filter for low-earth-orbit formation estimation using cdgps. *NAVIGATION*, *50*(2), 79–93. URL: https://onlinelibrary.wiley.com/doi/abs/10.1002/j.2161-4296.2003.tb00320.x. doi:https://doi.org/10.1002/j.2161-4296.2003.tb00320.x.

Capuano, V., Harvard, A., & Chung, S.-J. (2022). On-board cooperative spacecraft relative navigation fusing gnss with vision. *Progress in Aerospace Sciences*, *128*, 100761. URL: https://www.sciencedirect.com/science/article/pii/S0376042121000646. doi:https://doi.org/10.1016/j.paerosci.2021.100761.

Carter, T. E. (1998). State transition matrices for terminal rendezvous studies: Brief survey and new example. *Journal of Guidance, Control, and Dynamics*, *21*(1), 148–155. URL: https://doi.org/10.2514/2.4211. doi:10.2514/2.4211.

Centre National d'Études Spatiales, European Commission, & European Space Agency (2011). *User guide for EGNOS application developers : ED 2.0, 15/12/2011*. Publications Office. URL: https://op.europa.eu/en/publication-detail/-/publication/9028327b-8122-4cfc-97a8-4243c7d78039. doi:doi/10.2769/22157.

Ceva, J. G., & Parkinson, B. W. (1993). Multipath interference in orbiting receivers due to earth surface reflections. In *Proceedings of the 6th International Technical Meeting of the Satellite Division of The Institute of Navigation (ION GPS 1993)* (pp. 1557–1563). Salt Lake City, UT. URL: https://www.ion.org/publications/abstract.cfm?articleID=4294.

Clohessy, W. H., & Wiltshire, R. S. (1960). Terminal guidance system for satellite rendezvous. *Journal of the Aerospace Sciences*, *27*(9), 653–658. URL: https://doi.org/10.2514/8.8704. doi:10.2514/8.8704.

Correa-Muños, N. A., & Cerón-Calderón, L. A. (2018). Precision and accuracy of the static GNSS method for surveying networks used in civil engineering. *Ingeniería e Investigación*, *38*(1), 52–59. doi:10.15446/ing.investig.v38n1.64543.

Crisan, A. M., Martian, A., Cacoveanu, R. et al. (2020). Distance estimation in OFDM inter-satellite links. *Measurement*, *154*, 107479. URL: https://www.sciencedirect.com/science/article/pii/S0263224120300166. doi:https://doi.org/10.1016/j.measurement.2020.107479.

D'Amico, S., Ardaens, J.-S., & Montenbruck, O. (2009). Navigation of formation flying spacecraft using gps: the prisma technology demonstration. In *Proceedings of the 22nd International Technical Meeting of the Satellite Division of The Institute of Navigation (ION GNSS 2009)* (pp. 1427–1441). Savannah, GA. URL: https://www.ion.org/publications/abstract.cfm?articleID=8552.

De Bakker, P. F., van der Marel, H., & Tiberius, C. C. (2009). Geometry-free undifferenced, single and double differenced analysis of single frequency gps, egnos and giove-a/b measurements. *GPS solutions*, *13*, 305–314. URL: https://link.springer.com/article/10.1007/s10291-009-0123-6. doi:https://doi.org/10.1007/s10291-009-0123-6.

De Florio, S., & D'Amico, S. (2010). Flight results from the autonomous navigation and control of formation flying spacecraft on the prisma mission. In *61st International Astronautical Congress (IAC)*. Prague, CZ: International Astronautical Federation. URL: https://iafastro.directory/iac/archive/browse/IAC-10/C1/5/8016/.

D'Errico, M. (2012). *Distributed space missions for earth system monitoring* volume 31. (1st ed.). Springer Science & Business Media. URL: https://link.springer.com/book/10.1007/978-1-4614-4541-8. doi:10.1007/978-1-4614-4541-8.

European Space Agency (2022). SWARM mission data. https://earth.esa.int/eogateway/missions/swarm/data.

Giralo, V., & D'Amico, S. (2021). Precise real-time relative orbit determination for large-baseline formations using gnss. In *Proceedings of the 2021 International Technical Meeting of The Institute of Navigation* (pp. 366–384). URL: https://www.ion.org/publications/abstract.cfm?articleID=17839. doi:10.33012/2021.17839.

Guo, F., & Zhang, X. (2012). Real-time clock jump detection and repair for precise point positioning. In *Proceedings of the 25th International Technical Meeting of the Satellite Division of The Institute of Navigation (ION GNSS 2012)* (pp. 3077–3088). Nashville, TN. URL: https://www.ion.org/publications/abstract.cfm?articleID=10487.

Izenman, A. J. (2008). *Modern multivariate statistical techniques: Regression, classification and manifold learning*. (1st ed.). Springer New York, NY. URL: https://link.springer.com/book/10.1007/978-0-387-78189-1. doi:10.1007/978-0-387-78189-1.

Jazwinski, A. (1970). Applications of linear theory. In A. H. Jazwinski (Ed.), *Stochastic Processes and Filtering Theory* chapter 8. (pp. 266–331). Elsevier volume 64 of *Mathematics in Science and Engineering*. URL: https://www.sciencedirect.com/science/article/pii/S0076539209603775. doi:https://doi.org/10.1016/S0076-5392(09)60377-5.

Klobuchar, J. A. (1987). Ionospheric time-delay algorithm for single-frequency GPSusers. *IEEE Transactions on Aerospace and Electronic Systems*, *AES-23*(3), 325–331. URL: https://ieeexplore.ieee.org/document/4104345. doi:10.1109/TAES.1987.310829.

Komjathy, A., & Langley, R. (1996). An assessment of predicted and measured ionospheric total electron content using a regional GPS network. In *Proceedings of the national technical meeting of the Institute of Navigation* (pp. 615–624). Santa Monica, CA: Citeseer. URL: https://www.ion.org/publications/abstract.cfm?articleID=438.

Kroes, R., Montenbruck, O., Bertiger, W. et al. (2005). Precise grace baseline determination using GPS. *GPS Solutions*, *9*(1), 21–31. URL: https://link.springer.com/article/10.1007/s10291-004-0123-5. doi:10.1007/s10291-004-0123-5.

Le, A., & Tiberius, C. (2003). GPS standard positioning service: how good is it? *European Journal of Navigation*, *1*(2), 21–27.

Lear, W. (1988). *GPS navigation for low-earth orbiting vehicles, 1st revision*. Technical Report 87-FM-2, JSC-32,031 NASA Lyndon B. Johnson Space Center, Mission planning and analysis division.

Leick, A., Rapoport, L., & Tatarnikov, D. (2015). GNSS positioning approaches. In *GPS Satellite Surveying* chapter 6. (pp. 257–399). John Wiley & Sons, Ltd. URL: https://onlinelibrary.wiley.com/doi/abs/10.1002/9781119018612.ch6. doi:https://doi.org/10.1002/9781119018612.ch6.

Leung, S., & Montenbruck, O. (2005). Real-time navigation of formation-flying spacecraft using global-positioning-system measurements. *Journal of Guidance, Control, and Dynamics*, *28*(2), 226–235. URL: https://doi.org/10.2514/1.7474. doi:10.2514/1.7474.

Lopez, J. L. S. (2017). *A general architecture for autonomous navigation of unmanned aerial systems*. Ph.D. thesis Technical University of Madrid Madrid, ES. URL: https://dialnet.unirioja.es/servlet/tesis?codigo=156146.

Luxspace (2021). Triton-X, The high-performance microsatellite platform. Brochure. URL: https://luxspace.lu/wp-content/uploads/2021/08/Triton-X_Heavy_Brochure.pdf.

Mahfouz, A., Mezio, D., Dalla-Vedova, F. et al. (2022). Relative state estimation for leo formations with large inter-satellite distances using single-frequency GNSS receivers. In *Proceedings of the 11th International Workshop on Satellite Constellations & Formation Flying*. Milan, IT.

Montenbruck, O., Ebinuma, T., Lightsey, E. et al. (2002). A real-time kinematic gps sensor for spacecraft relative navigation. *Aerospace Science and Technology*, *6*(6), 435–449. URL: https://www.sciencedirect.com/science/article/pii/S1270963802011859. doi:https://doi.org/10.1016/S1270-9638(02)01185-9.

Park, H.-E., Park, S.-Y., Kim, S.-W. et al. (2013). Integrated orbit and attitude hardware-in-the-loop simulations for autonomous satellite formation flying. *Advances in Space Research*, *52*(12), 2052–2066. URL: https://www.sciencedirect.com/science/article/pii/S0273117713005784. doi:https://doi.org/10.1016/j.asr.2013.09.015.

Park, J.-I., Park, H.-E., Park, S.-Y. et al. (2010). Hardware-in-the-loop simulations of GPS-based navigation and control for satellite formation flying. *Advances in Space Research*, *46*(11), 1451–1465. URL: https://www.sciencedirect.com/science/article/pii/S0273117710005260. doi:https://doi.org/10.1016/j.asr.2010.08.012.

Peng, Y., Scales, W. A., Esswein, M. C. et al. (2019). Small satellite formation flying simulation with multi-constellation GNSS and applications to future multi-scale space weather observations. In *Proceedings of the 32nd International Technical Meeting of the Satellite Division of The Institute of Navigation (ION GNSS+ 2019)* (pp. 2035–2047). Miami, Florida. URL: https://www.ion.org/publications/abstract.cfm?articleID=16883. doi:10.33012/2019.16883.

Peng, Y., Scales, W. A., & Lin, D. (2021). GNSS-based hardware-in-the-loop simulations of spacecraft formation flying with the global ionospheric model TIEGCM. *GPS Solutions*, *25*, 1–14. URL: https://link.springer.com/article/10.1007/s10291-021-01099-x. doi:10.1007/s10291-021-01099-x.

Rao, A. (2006). Kinematics. In *Dynamics of particles and rigid bodies: a systematic approach* chapter 2. (pp. 27–130). Cambridge University Press. URL: https://www.cambridge.org/eg/academic/subjects/engineering/solid-mechanics-and-materials/dynamics-particles-and-rigid-bodies-systematic-approach?format=HB&isbn=9780521858113.

Rao, G. S. B. (2008). Ionospheric delay estimation for improving the global

positioning system position accuracy. *IETE Journal of Research*, *54*(1), 23–29. URL: https://doi.org/10.1080/03772063.2008.10876178. doi:10.1080/03772063.2008.10876178.

Renga, A., Causa, F., Tancredi, U. et al. (2018). Accurate ionospheric delay model for real-time GPS-based positioning of leo satellites using horizontal vtec gradient estimation. *GPS Solutions*, *22*(2), 1–14. URL: https://link.springer.com/article/10.1007/s10291-018-0710-5. doi:10.1007/s10291-018-0710-5.

Tancredi, U., Allende-Alba, G., Renga, A. et al. (2015). Relative positioning of spacecraft in intense ionospheric conditions by gps. *Aerospace Science and Technology*, *43*, 191–198. URL: https://www.sciencedirect.com/science/article/pii/S1270963815000772. doi:https://doi.org/10.1016/j.ast.2015.02.020.

Tancredi, U., Renga, A., & Grassi, M. (2014). Real-time relative positioning of spacecraft over long baselines. *Journal of Guidance, Control, and Dynamics*, *37*(1), 47–58. URL: https://doi.org/10.2514/1.61950. doi:10.2514/1.61950.

Varrette, S., Bouvry, P., Cartiaux, H. et al. (2014). Management of an academic hpc cluster: The ul experience. In *Proc. of the 2014 Intl. Conf. on High Performance Computing & Simulation (HPCS 2014)* (pp. 959–967). Bologna, Italy: IEEE. URL: https://ieeexplore.ieee.org/abstract/document/6903792. doi:https://doi.org/10.1109/HPCSim.2014.6903792.

Woods, J. O., & Christian, J. A. (2016). Lidar-based relative navigation with respect to non-cooperative objects. *Acta Astronautica*, *126*, 298–311. URL: https://www.sciencedirect.com/science/article/pii/S0094576515301661. doi:https://doi.org/10.1016/j.actaastro.2016.05.007. Space Flight Safety.

Yunck, T. P. (1993). Coping with the atmosphere and ionosphere in precise satellite and ground positioning. In *Environmental Effects on Spacecraft Positioning and Trajectories* chapter 1. (pp. 1–16). American Geophysical Union (AGU). URL: https://agupubs.onlinelibrary.wiley.com/doi/abs/10.1029/GM073p0001. doi:https://doi.org/10.1029/GM073p0001.